Improved anti-noise adaptive long short-term memory neural network modeling for the robust remaining useful life prediction of lithium-ion batteries.

WANG, S., FAN, Y., JIN, S., TAKYI-ANINAKWA, P. and FERNANDEZ, C.

2023

Improved anti-noise adaptive long short-term memory neural network modeling for the robust remaining useful life prediction of lithium-ion batteries

Shunli Wang[12*], Yongcun Fan[2], Siyu Jin[3], Paul Takyi-Aninakwa[1], Carlos Fernandez[4]

[1] Chengdu University of Information Technology, Chengdu 610225, China; [2] School of Information Engineering, Southwest University of Science and Technology, Mianyang 621010, China; [3] Department of Energy Technology, Aalborg University, Pontoppidanstraede 111 9220 Aalborg East, Denmark; [4] School of Pharmacy and Life Sciences, Robert Gordon University, Aberdeen AB10-7GJ, UK.

Abstract: Safety assurance is essential for lithium-ion batteries in power supply fields, and the remaining useful life (RUL) prediction serves as one of the fundamental criteria for the performance evaluation of energy and storage systems. Based on an improved dual closed-loop observation modeling strategy, an improved anti-noise adaptive long short-term memory (ANA-LSTM) neural network with high-robustness feature extraction and optimal parameter characterization is proposed for accurate RUL prediction. Then, an adaptive state parameter feedback correction strategy is constructed through multiple feature collaboration with its internal coupling mechanism characterization, which considers varying current rates, ambient temperatures, and other influencing parameters. Subsequently, a collaborative multi-parameter optimization is carried out along with the model training and meta-structure fine-tuning. Compared with other optimal existing methods, the maximum root mean square error decreases by 51.80%, the mean absolute error reduces by 26.95%, the maximum mean absolute percentage error decreases by 33.87%, and the *R*-squared increases by 4.11%. The established multiple-feature collaboration model realizes multi-scale parameter optimization and robust RUL prediction, thus advancing the industrial application of lithium-ion batteries.

Keywords: lithium-ion battery; remaining useful life prediction; anti-noise adaptive long short-term memory neural network; multi-feature collaboration; adaptive feedback correction

***Corresponding author**: Shunli Wang, Tel.: +86-0816-6089326, wangshunli@swust.edu.cn.

Highlights:

- An improved ANA-LSTM model is built for RUL prediction of lithium-ion batteries
- Multiple feature collaboration is conducted for internal parameter characterization
- Adaptive feedback correction is established with the multi-feature collaboration
- Collaborative and multiple factors are optimized through meta-structure fine-tuning
- RUL prediction results show optimal MAE and RMSE of 0.390% and 0.604%, respectively

1. Introduction

With the continuous development of new energy vehicles and large-scale energy storage systems, lithium-ion batteries have become one of the most widely used energy storage systems due to their high energy and power densities, durability, low self-discharge, and long cycle life advantages. With deepening supply-side structural reform, lithium-ion batteries play an important role in energy transformation and industrial structure adjustment. For the third-generation battery-based energy storage system, reliability and safe management lay the foundation for effective and efficient industrial applications [1-4]. The high-accuracy remaining useful life (RUL) prediction promotes the infrastructure of battery systems as essential support in new energy development and management. Due to the inherent cell-to-cell differences and high nonlinearities as a result of the complex working conditions and multi-coupling characteristics, the robustness of the RUL prediction is difficult to improve, resulting in safety problems such as poor performance, rapid aging, and spontaneous combustion [5-7]. A constant change-point model is constructed to obtain the analytical results of the system reliability, lifetime distribution, and RUL prediction [8, 9]. Consequently, a robust and accurate RUL prediction is needed to ensure the long-term operation of the battery and the synchronous increasing dispersion among battery cells.

The key to solving the safety problem is to express the interaction between battery cells by effectively considering the coupling relationship between multiple state parameters and the polarization effect caused by frequent temperature variations. An efficient approach is proposed for battery health management for small-sized rotary-wing electric unmanned aerial vehicles (UAVs) using a constrained computational platform [10]. For the internally cascaded cells, the battery system has

the limitation of the complex series-parallel construction structure and strict safety requirements. Therefore, real-time monitoring and safety control should be conducted to ensure safety, reliable power supply, and durability. The physics-based prognostics are analyzed for lithium-ion batteries using nonlinear least square strategies with dynamic bounds [11]. Accurate state parameter prediction, including the core factors such as state of charge (SOC), state of health (SOH), state of power (SOP), and RUL, is the basis for ensuring safety and effective control [12, 13]. Based on the collaborative multi-feature extraction, the RUL prediction is realized, which plays a crucial role in improving the energy supply efficiency and promoting the high-quality development of the structural energy storage reform. Under the influence of the current magnification, ambient temperature, the number of cycles, and battery pack structure, the robustness of the RUL prediction model has significant guidance for energy enhancement.

The module-level single-factor mechanism is established to construct the optimization model suitable for the packing characteristics of multi-cell battery systems based on a single factor, which is extended to realize the combination of the modeling strategies. The dynamic model is used to express the time-dimension characteristics, which are integrated to supplement the physical distribution at a specific time point and typical state, effectively expressing the three-dimensional packing characteristics [14, 15]. To realize a robust RUL prediction, it is necessary to analyze and clarify the multi-factor mutual coupling mechanism on the working characteristics, including the coupling relationship and the prediction method for various state parameters [16-18]. The difference between battery cells is that their inherent characteristics affect the output parameters, including capacity, voltage, and internal resistance. Also, the causes are complex for the production influence and application process, including charging strategies, discharge modes, ambient temperature, and self-discharge effects, so the Bayesian hierarchical model-based prognostics are investigated for lithium-ion batteries. Over time, the parameter difference and coupling effect increase, which intensifies the impact on modeling parameters and state information variations.

The nonlinearity, strong time variability, and significant differences between different lithium-ion battery cells lead to the RUL prediction difficulty, which has made adaptive models become a research hotspot. Considering the SOH variational influence, a single particle modeling method is introduced to construct a time convolution network for RUL prediction with

optimized robustness [19]. Applying multiple uncertainty evaluation strategies, the RUL value is predicted online based on the *F*-distribution method for the extraction of multiple hidden state variables to realize the nonlinear drift fraction synchronously [20]. Multi-time-scale filtering and estimation algorithms, including support vector regression (SVR), Wiener process, particle filter (PF), and other optimized methods, have been used to achieve remarkable RUL prediction results [21-23]. The data-driven feature enhancement, adaptive optimization, and Gaussian regression methods are effective in the model parameter correction segments [24-26]. The RUL prediction is improved with the new index and score processing framework, combining the second-order central difference with grey modeling [27]. Based on the robust compound filter, the Gaussian regression and weighted averaging strategies are combined to form a new fusion for the RUL prediction, which is then combined with the nonlinear regression to construct a multi-time scale prediction framework [28]. The existing research mainly focuses on the battery cell under the single-factor influence rather than the perspective of the battery system considering the multiple-factor. However, the inaccurate RUL prediction problem has not been solved fundamentally.

Integration modeling and data-driven methods based on artificial intelligence (AI) have made great breakthroughs in simplifying the evaluation process of the complex electrochemical reactions in lithium-ion batteries. Deep learning (DL) and adaptive correction improve the energy efficiency and reliability of the battery systems effectively to predict the RUL value with robust characteristics [29-31]. The DL-based prediction method adopts different modeling mechanisms by combining them with time series analysis to effectively realize the RUL value [32]. The long short-term memory (LSTM), Gaussian process regression (GPR), and recurrent neural network (RNN) models are effective methods that can reflect the battery performance degradation trend with high accuracy [33, 34]. With the combination of LSTM and an enhanced self-correcting (ESC) model, the efficient RUL prediction model is constructed [35]. The intelligent DL-based data-driven strategy is used to effectively realize the real-time RUL prediction of lithium-ion batteries for UAVs by quantifying the uncertainties [36]. Based on the extreme learning machine (ELM) and feedforward neural network (FNN) with generalized learning (GL), an improved GL-ELM model is constructed, which has fast-learning and good-generalization performance advantages [37]. Based on the data-driven aging model, the transfer learning (TL) of the capacity degradation trend is realized by combining

it with Gaussian regression and the optimized deep convolution neural network (DCNN) strategies [34, 38-40]. The RUL value is predicted accurately, mainly based on the variations in voltage, current, and capacity rates during the charge-discharge processes.

The accurate prediction of state parameters, such as SOC, SOH, SOP, etc., plays an essential role in improving the RUL prediction accuracy of lithium-ion batteries. Compared with the easily measured parameters of voltage, current, and temperature, the working characteristics are reflected by the battery state factors [41]. A large number of state parameter prediction models have been constructed for high-precision RUL prediction with high robustness and anti-interference ability [42]. The influencing factors of the aging characteristics are analyzed under various working conditions, according to which the RUL prediction strategy is explored in combination with the state parameters. A full theoretical analysis is conducted for the collaborative state parameter prediction [43-45]. Considering the changing laws of key state parameters, the iterative calculation provides strong support for the construction of accurate RUL prediction models [46-48]. The prediction algorithms are mainly constrained by short-time scale parameters such as voltage, current, temperature, and SOC instead of considering the influence of long-timescale parameters, such as capacity, internal resistance, and SOH [49]. The research on the action mechanism of inter-cell difference, multi-time scale constraint, and parameter coupling is still immature, so the RUL prediction under complex working conditions needs to be further studied [50]. The DL-based theory is an essential development trend to improve the RUL prediction robustness with the improvement strategy of adaptive algorithms.

The existing RUL prediction methods under various application conditions are insufficient under several working conditions and characteristics where the mathematical expression and comprehensive evaluation of several potential characteristics are not considered [51-53]. The model-based and data-driven collaborative state prediction strategies based on multi-boundary fusion need further analysis. Modular circuit characterization methods have been introduced to improve RUL prediction accuracy under complex working conditions [54, 55]. Multi-time scale prediction models are established with the state-space model using the characteristic information of external measurable parameters, in which correction strategies are employed for the influencing factors, including the internal connected cell-to-cell difference.

Based on the urgent needs of the above research, this paper proposes an improved anti-noise adaptive long short-term memory (ANA-LSTM) neural network coupled with an adaptive feedback correction strategy, which is constructed through multiple feature collaboration to achieve a high-precision RUL prediction. The main contributions of this research are described as follows. Firstly, the composite and robust prediction algorithms are analyzed in combination with the urgent application requirements. Then, the battery performance is clarified by the influencing mechanism analysis of multi-time scale constraints and cell differences. Secondly, based on the compound modeling strategy and data-driven multi-factor collaborative state prediction framework, an anti-noise adaptive iterative calculation procedure is constructed with a feedback correction to improve the prediction accuracy and robustness. Finally, the collaborative prediction algorithm is designed for key state parameters. The multi-objective hierarchical composite prediction model is constructed for the RUL prediction under multivariable coupling influence, which effectively supports the intelligent control and active core state parameter protection of the battery system.

2. Mathematical analysis

The battery characteristics are analyzed by clarifying the coupling mechanism between multiple variables, which solves the inaccurate characterization problem in the RUL prediction process under complex working conditions. The energy attenuation influencing mechanism is revealed, according to which the differentiated prediction is realized to establish the functional relationship between the state parameters and the RUL value. A robustness RUL prediction strategy is carried out that is formulated according to the established research objectives. The life attenuation mechanism is revealed by establishing the functional description of the coupling relationship between key parameters to realize the robust prediction. Then, an optimized multi-index state prediction algorithm is formed by the in-depth data-driven mechanism, according to which an accurate RUL prediction model is constructed and realized when it is combined with the key parameter optimization and feedback correction.

2.1. Multiple-stage fusion model-based RUL prediction framework

Based on the multi-stage composite modeling, multi-scale constrained anti-noise analysis, multi-boundary distributed prediction, and multi-factor coupling parameter optimization, the collaborative aging characteristics are analyzed to obtain the anti-noise parameter identification and expansion strategies. The phased optimization is conducted to describe the cell-to-cell difference to improve universality and reduce complexity, establishing a highly adaptive compound equivalent circuit model (CECM). Based on the self-optimizing strategy, the adaptive prediction and correction strategies are employed to construct a robust RUL prediction model. The charge-discharge characterization and parameter performance expansion are conducted, in which the multi-factor coupling mechanism expansion is realized for different packing modes and the fusion of different SOC levels, respectively. After the capacity and internal resistance screening, the cell-to-cell performance difference turns out to be relatively small. The basic data charge-discharge characteristics are obtained with the series and parallel expansion. Combined with the variation law of multiple influencing factors, the adaptive CECM is constructed. The modular equivalent strategies are introduced to characterize the polarization effect, self-discharge influence, and charge-discharge difference. The effects of different combining optimization methods are evaluated along with the application scenarios, improving the ECM theory and establishing a multi-stage fusion model framework, as shown in Figure 1.

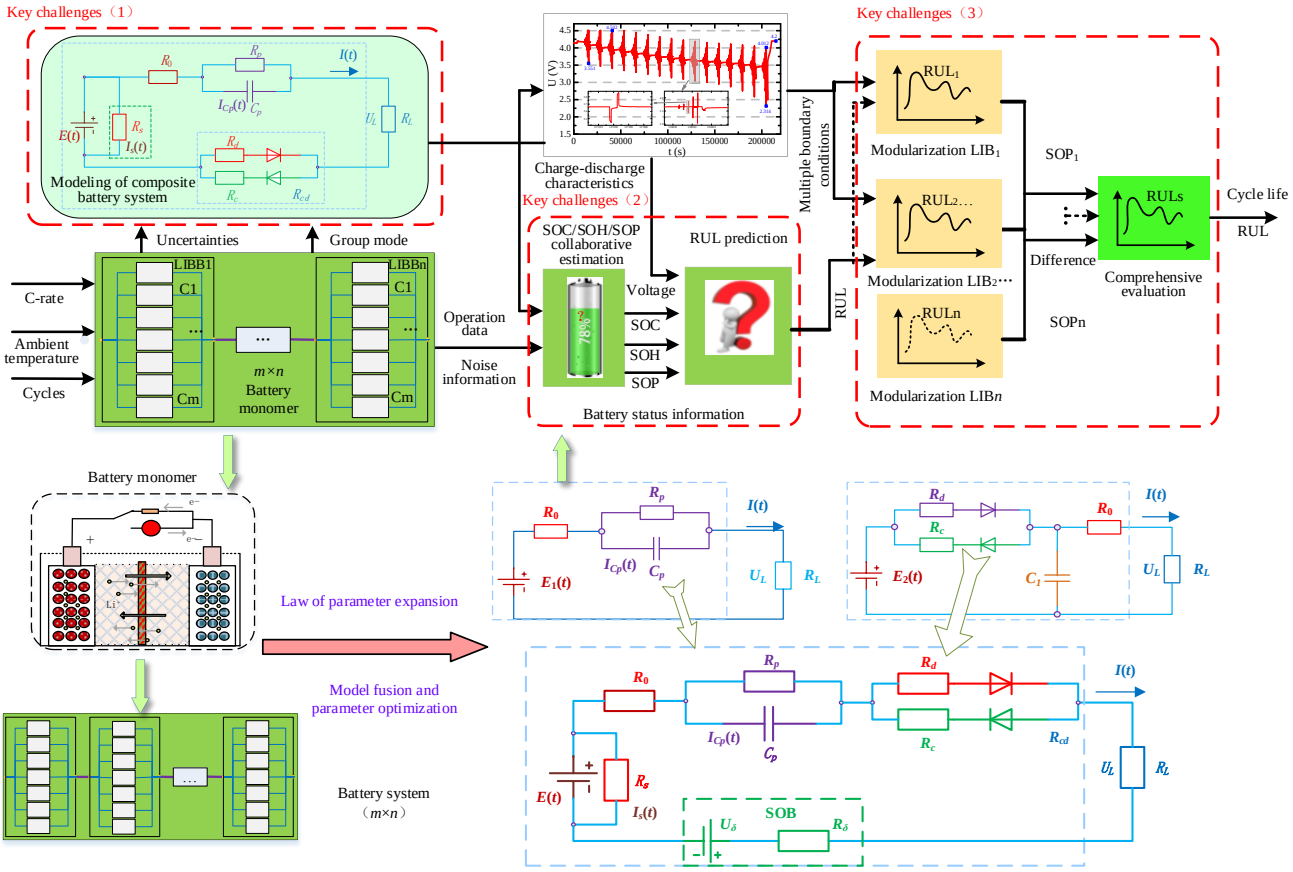

Figure 1. Multi-stage fusion model framework for battery characterization

In Figure 1, $E(t)$ is the open-circuit voltage (OCV) value; R_s reflects the self-discharge resistance phenomenon; R_0 is the ohmic resistance effect and describes the instantaneous voltage variations during the charge-discharge process. The resistor-capacitor (RC) parallel circuit simulates the polarization effect, R_p is the polarization resistance, and C_p is polarization capacitance. R_c and R_d are the internal resistance differences during the charge and discharge processes, respectively. U_δ and R_δ characterize the equilibrium influence that describes the difference between internal cascade battery cells. The output voltage variation of the constant current-constant voltage (CC-CV) stages is characterized by U_L and $I(t)$ is the current flowing through the battery. When combined with the working characteristics and optimization strategies, the physical distribution is expanded in both time and space dimensions. Then, a complete model is constructed by integrating static and dynamic characteristics to expound the multi-physical quantity action mechanism and establish the effective mathematical state-space model.

2.2. Anti-noise adaptive multi-time scale cooperative state estimation

Based on the adaptive CECM, the state information is defined to construct the optimized objective function. After that, the collaborative state prediction procedure is designed that is adaptive to the complex time-varying conditions when the noise is uncertain to accurately predict the RUL value through data fusion and feedback correction. An adaptive estimator is constructed for the nonlinear parameters to obtain the time-varying statistical information of measurement and modeling noises synchronously. The influencing degree of environmental conditions is introduced into the mathematical expression to construct the state of balance (SOB) weighting factor, and the initial value is preset for real-time correction. Through the numerical representation of the cell-to-cell difference, the state parameters are optimized to improve the modeling accuracy that is combined with the variance and coefficient evaluation. The coefficients of variation θ and ε are introduced to characterize SOB, as shown in Equation (1).

$$SOB = \varepsilon = \theta^2 = \frac{1}{n}\sum_{i=1}^{n}\left(\frac{U_{c_i} - E\left(U_c\right)}{E\left(U_c\right)}\right)^2 \tag{1}$$

In Equation (1), ε is the voltage difference between battery cells; θ is the coefficient of the cell-to-cell variation; U_{c_i} is the measured voltage of the ith battery cell; n is the number of battery cells. Based on the framework of the constructed adaptive state prediction model, the influencing mechanism of SOB is introduced into the modeling process, in which both the voltage and internal resistance changes are considered to characterize the influence of the cell-to-cell differences. Consequently, the correction goal is achieved to obtain the accurate expression, as shown in Equation (2).

$$\begin{cases} U_\delta(k) = \varepsilon * U_{OC}(k) = \dfrac{1}{n}\displaystyle\sum_{i=1}^{n}\left[\frac{U_{c_i}(k) - E\left(U_c(k)\right)}{E\left(U_c(k)\right)}\right]^2 * U_{OC}(k) \\ R_\delta(k) = \varepsilon * R_0(k) = \dfrac{1}{n}\displaystyle\sum_{i=1}^{n}\left[\frac{U_{c_i}(k) - E\left(U_c(k)\right)}{E\left(U_c(k)\right)}\right]^2 * R_0(k) \end{cases} \tag{2}$$

In Equation (2), the influence of SOB is described mathematically and integrated into the iterative calculation process. Based on the typical parameter impact values on the prediction results, the dynamic effects are considered effectively,

including ambient temperature, aging characteristics, and current magnification. Consequently, TL strategies are introduced to obtain the pre-training of the prediction network and the fine-tuning of neuron structure. On this basis, multi-task training and optimization are carried out to improve the robustness of the prediction through iterative calculation with adaptability. Consequently, a dual closed-loop DL-based observation framework is constructed, as shown in Figure 2.

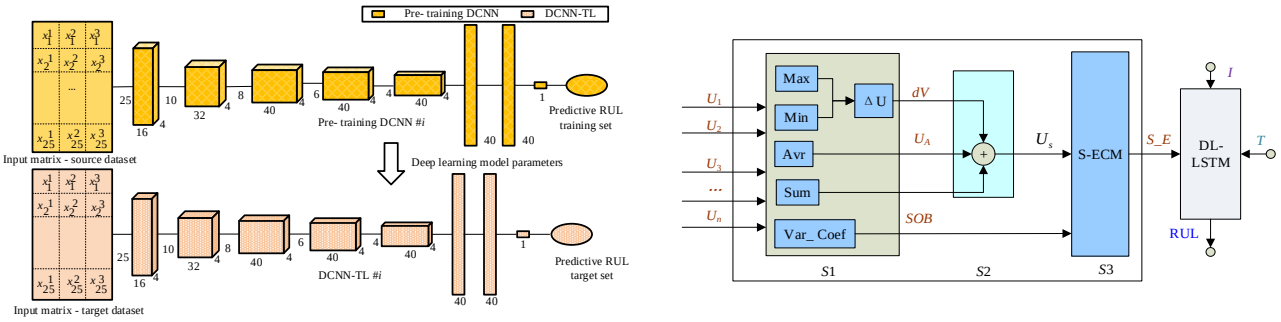

(a) Framework of the dual closed-loop DL-based observation model

(b) Framework of the RUL prediction model

Figure 2. The dual closed-loop DL-based observation and RUL prediction model

In Figure 2 (a), the dual closed-loop DL-based observation and RUL prediction methods in this paper contain two closed-loop structures, including pre-training DCNN and CNN-TL. The TL strategy is applied, in which the source domain points to the training data set are transferred to the target domain points to the test dataset. The training data part is selected, and the battery attenuation characteristics are extracted to predict the battery capacity, which reduces the computational burden of the algorithm. The coupling mechanism between SOC, SOH, and SOP is clarified by taking the statistical results as input factors. The SOC value is used as the intermediate state, and each state's information is taken as input with each other to realize the iterative calculation with strong adaptability and anti-noise ability, constructing a multi-state parameter collaborative prediction model. The adaptive prediction ability is improved by the real-time correction of voltage signals. The intermediate parameters of mean voltage U_a, variation coefficient SOB, and voltage change rate dV are calculated iteratively. The equivalent voltage of a single unit is obtained by calculating the effective state function of the adaptive CECM. A DL-based iterative calculation model is constructed for the robust RUL prediction, in which the unit voltages of U_1, U_2, U_3,..., and U_n are measured in real-time. Then, the basic operations, such as difference, mean, and variance, are carried out in step *S*1. The key parameters are fused and calculated in step *S*2, which are introduced into the model in step *S*3 to obtain

the state-space equation (*S_E*). Also, the current I under the working condition influence is taken as the main input parameter, and the temperature signal T is taken as the correction factor. The DL-LSTM iterative calculation is carried out recursively to obtain the RUL value and the correction factor for the implementation procedure.

Based on the ECM and state-space model, the particularity is revealed with the influencing factors of the key parameters. The correction strategy of the key parameters is obtained by the theoretical analysis of the influencing factors, including the charge-discharge current, ambient temperature, cycle life, self-discharge current rate, and cell-to-cell difference. Based on the multi-input and high nonlinearity characteristics, the transformation functions are obtained by considering both the mean and covariance. The dynamic random vector model is constructed to express the approximate Gaussian distribution of the sampling data points. The DL theory is also introduced to improve the adaptability of the prediction model for complex working conditions. The influencing factors of multi-time scale constraints are clarified, including the closed-circuit voltage, output current, ambient temperature, SOC, SOH, SOP, and RUL variations.

Combined with the noise correction strategy, a multi-constraint collaborative state prediction algorithm is modeled to estimate the RUL value. The influencing factors of the inter-unit differences in the prediction process are combined with those of the multi-time scale constraints to construct an inter-unit differential corrector by reliability reasoning. The correcting coefficient is multiplied by the referenced value for the RUL prediction and the reliable correction of inter-unit differences. The algorithm structure is modeled and realized, as shown in Figure 3.

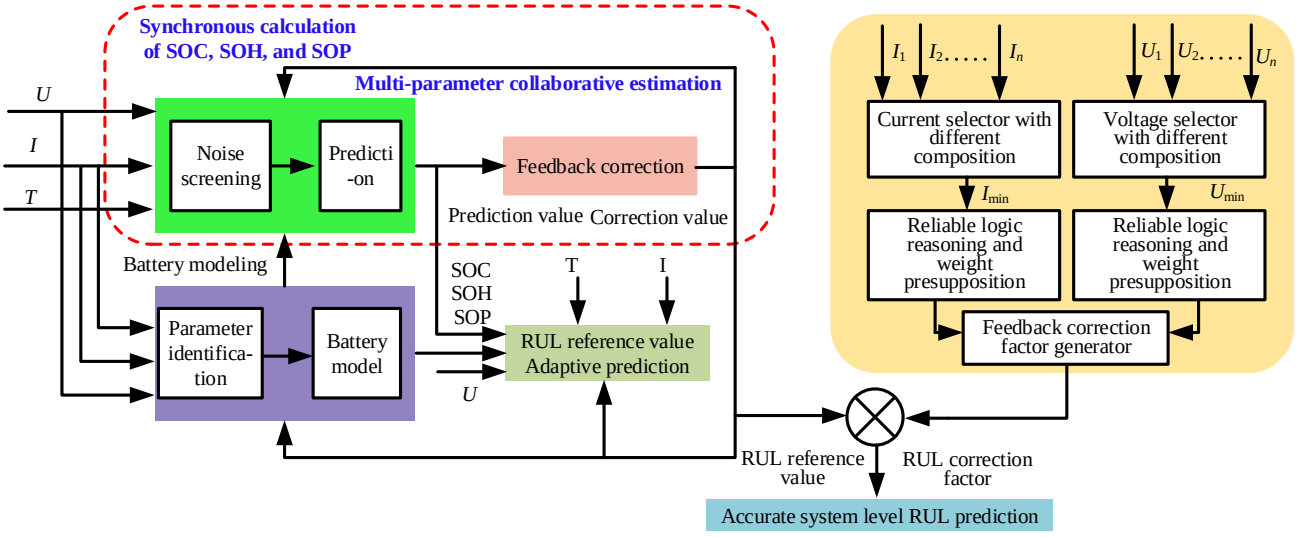

Figure 3. Multi-time scale RUL prediction based on the cell-to-cell difference feedback correction

In Figure 3, various state parameters are taken into consideration, including CCCV, SOC, SOH, SOP, and RUL values. Multi-standard comprehensive error evaluation methods are introduced to verify the accuracy and robustness of the proposed method. If the expected accuracy is not achieved, the prediction calculation process is iterated to further improve the noise correction, collaborative state estimations, and multi-constraint RUL prediction. The multi-time scale and multi-objective state parameter collaborative prediction are conducted using the intelligent feedback correction strategy.

2.3. Power supply update based on DCNN-TL and LSTM strategies

The constraint mechanism of each boundary condition is established to realize the modular RUL prediction method through a logic DL-based iterative calculation. The *n*-dimensional target sampling point values are obtained by the state update. The prediction data set is obtained based on the calculation rules, which are transferred to the nonlinear function synchronously. Based on the state-space model and measurement noise correction factor, a new data set is resampled to improve the real-time adaptive correction effect. The framework of the optimal RUL prediction method through a logic DL-based iterative calculation with the LSTM model is shown in Figure 4.

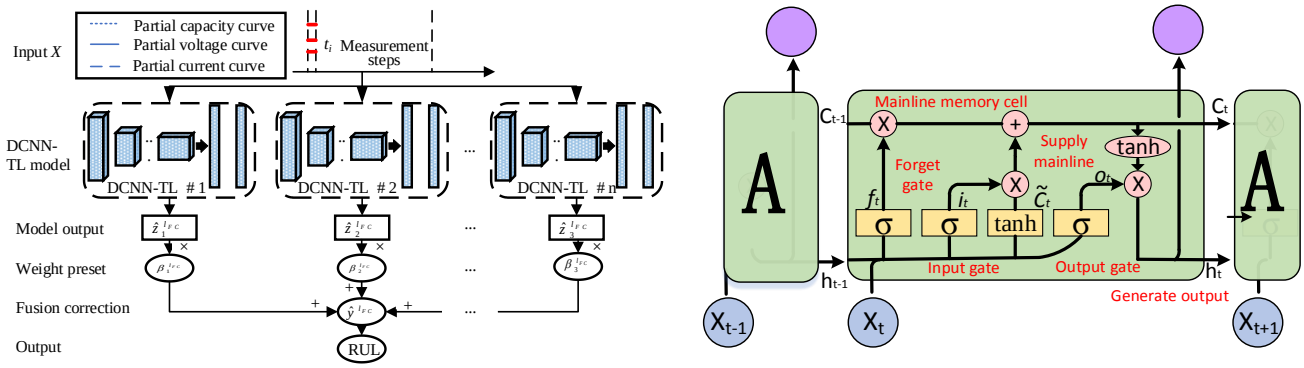

(a) Iterative RUL prediction based on DCNN-TL strategy (b) LSTM framework

Figure 4. The structure of the DCNN-TL strategy and LSTM-based RUL prediction method

In Figure 4 (a), the performance attenuation mechanism is introduced by considering the aging characteristics, including temperature, current magnification, depth of discharge, and SOC variations. The state-space model and data-driven mechanism are combined to optimize the parameter identification effects for accurate prediction outputs. Regarding LSTM as a black box, the single cell can be divided into several key units, which are the memory cell, forget, input, and output gates.

The input parameters are the hidden state h_{t-1} at a time point $t-1$, and the input data x_t at a time point t. The mainline of the memory cell state from the previous C_{t-1} to the current time point C_t, and the final processed output information for a single layer h_t.

The input information of the hidden layer h_{t-1} and input x_t are used as the main input information and they control the three gates. The three gates in the LSTM model include a forget gate f_t, an input gate i_t, and an output gate o_t to protect and control the memory cell. The forget gate f_t determines which parameter information from the current input x_t and previously hidden state h_{t-1} of the memory cell to keep or discard through the sigmoid layer by directing each piece of information to either 1 or 0, respectively. The mathematical expression for the forget gate is shown in Equation (3).

$$f_t = \sigma\left(W_f h_{t-1} + W_f x_t + b_f\right) \tag{3}$$

The new information to be stored in the memory cell is determined by the input gate i_t (cell status update). It takes information provided by the current input x_t and previously hidden state h_{t-1} and processes it using the sigmoid and $tanh$ layers. The sigmoid layer first chooses which current input i_t data should be used to update the cell. The $tanh$ layer subsequently generates a C_t cell state vector, which is then added to the cell state. These sigmoid and $tanh$ layers collaborate to determine what information is kept in the cell state, as mathematically expressed in Equation (4).

$$\begin{cases} i_t = \sigma\left(W_i h_{t-1} + W_i x_t + b_i\right) \\ \tilde{C}_t = tanh\left(W_c h_{t-1} + W_c x_t + b_c\right) \end{cases} \tag{4}$$

To update the memory cell for a new cell state C_t, the input i_t and cell state vector $\tilde{C}_t$ are multiplied and added to the previous cell state using the point-by-point multiplication of C_{t-1} and f_t, as mathematically expressed in Equation (5).

$$C_t = f_t \cdot C_{t-1} + i_t \cdot \tilde{C}_t \tag{5}$$

Based on filtered information from the new cell state C_t, the output gate o_t selects the information for the next hidden state or test output. First, the sigmoid layer specifies which information about the cell state should be the output. Second, the $tanh$ layer regulates the information from the new cell state C_t, which ranges between –1 and 1. The output o_t is then multiplied by the output of the sigmoid layer to obtain the new hidden state h_t. Equation (6) shows the mathematical expressions for the output gate o_t and the new hidden state h_t.

$$\begin{cases} o_t = \sigma\left(W_o h_{t-1} + W_o x_t + b_o\right) \\ h_t = tanh\left(C_t\right) \cdot o_t \end{cases} \tag{6}$$

In Equation (6), σ is the sigmoid layer which aids the LSTM model in updating or dropping information between 0 and 1. Also, x_t is the current data input, and h_{t-1} represents the previous time point's hidden state or output. The $tanh$ is a hyperbolic tangent function that prevents fading by controlling the information flowing through the model between –1 and 1. W_f, W_i, W_c, and W_o that are weights associated with the forgetting, input, cell, and output gates. Furthermore, the forgetting, input, cell, and output gates, which have bias vectors of b_f, b_i, b_c, and b_o to boost the flexibility of the network that is adaptive to the training data.

From Equation (6), the weight coefficient of the output gate is updated by the forward propagation and the backpropagation, which are optimized iteratively by conducting the error term transmission for the time sequence. In the early prediction stage, a multivariable hidden Markov model (HMM) is constructed to realize the multi-factor weighting correlation on the aging characteristics, state parameters, and RUL variation. It is used to achieve accurate short-term prediction and error correction. For the later prediction process, the long-term and short-term memory time series are combined by the LSTM model. The dual feedback correction is conducted for the feature and time series so that the correlation of time dependence is realized to improve the prediction accuracy. The correlation is extracted between the internal characteristic parameters, environmental conditions, and operation data, according to which the real-time correction is realized for the auxiliary information, independent key time point selection, and mathematical expression enhancement. Consequently, the prediction effect and stability are improved for a long time series, along with the prediction algorithm design based on ECM and data-driven fusion strategies.

2.4. Feature decomposition preprocessing and iterative RUL prediction

The capacity attenuation is usually accompanied by capacity regeneration, which is due to the slowing down of the internal electrochemical reactions after shelving, resulting in a slight recovery along with the capacity regeneration and attenuation trend, affecting the RUL prediction. The fast Fourier transform, wavelet, and Hilbert transform strategies are

combined to express the nonlinear characteristics with strong adaptability without setting the basic function and feasible decomposition layer. Consequently, the measured parameters are well-decomposed and distinguished between capacity regeneration and attenuation. The battery capacity is converted into components of different frequencies, including the eigenmode function and residual components. Therefore, the original capacity data $C(t)$ is mathematically expressed, as shown in Equation (7).

$$C(t) = \sum_{j=1}^{n} c_j(t) + r_n(t) \tag{7}$$

In Equation (7), $c_j(t)$ is the *j*th eigenmode function that is used to describe the capacity regeneration; $r_n(t)$ is the residual component to express the real degradation process; n is the number of the eigenmode functions. The decomposition is completed based on the mathematical expression, as shown in Equation (8).

$$\sum_{t=1}^{n} \frac{\left[c_{j-1}(t) - c_j(t)\right]^2}{c_{j-1}^2(t)} \leq \delta, j = 1, 2, \cdots, n \tag{8}$$

In Equation (8), n is the cyclic charge-discharge number; δ is the ending judgment parameter with a value of 0.5 for the RUL prediction procedure. The SOH level is described by the capacity degradation characteristics, according to which the end-of-life (EOL) value is calculated and taken as 80% of the rated capacity. The mathematical expressions for the SOH in terms of capacity and EOL are shown in Equation (9).

$$SOH = \frac{C_n}{C_0} \times 100\% \Rightarrow EOL = C_0 \times 0.8 \tag{9}$$

In Equation (9), C_0 is the rated capacity; C_n is the real-time capacity for the cyclic charge-discharge number of n. The RUL value is characterized as the number of the remaining cyclic charge-discharge, as shown in Equation (10).

$$RUL = n_{T\_EOL} - n_t \Rightarrow \widehat{RUL} = n_{P\_EOL} - n_t \tag{10}$$

In Equation (10), n_{T_EOL} is the total number of cycles; n_t is the current number of cycles; $\widehat{RUL}$ is the predicted RUL value; n_{P_EOL} is the predicted number of cycles to the EOL value of the battery. To realize an accurate RUL prediction, the prediction model is constructed with a multiple-to-one structure for both SOH estimation and RUL prediction. The training model is constructed using the current and voltage as input parameters, as shown in Equation (11).

$$c_{ji} = LSTM \begin{cases} I_{ji}^1, I_{ji}^2, \cdots, I_{ji}^n \\ U_{ji}^1, U_{ji}^2, \cdots, U_{ji}^n \end{cases} \tag{11}$$

In Equation (11), c_{ji} is the jth cell in the ith cycle; I_{ji}^{n} and U_{ji}^{n} are the respective measured current and voltage values at the final time point in the cyclic charge-discharge process. For each parameter, n is the total number of the sampling data points used as the input vectors. The trained ANA-LSTM model is trained to estimate the battery capacity, as shown in Equation (12).

$$\hat{c}_{ji} = LSTM \begin{cases} I_{ji}^{1}, I_{ji}^{2}, \cdots, I_{ji}^{n} \\ U_{ji}^{1}, U_{ji}^{2}, \cdots, U_{ji}^{n} \end{cases} \tag{12}$$

In Equation (12), $\hat{c}_{ji}$ is the estimated capacity for the jth cell and ith cycle. Then, the SOH value is calculated accordingly. For the RUL prediction, another LSTM sub-model is constructed using the one-to-one structure. The historical capacity is taken as the input parameter, and the predicted capacity value in the next cycle is taken as the output. The SOH sequence is constructed and the w feature is introduced to predict the $w+1$ value by taking w as the sliding window. A decomposition is conducted to preprocess the data sequence. The RUL prediction model is established to overcome the fluctuations in the SOH sequence that influence the prediction, as shown in Equation (13).

$$\begin{cases} s_{t+1} = LSTM\{s_{t-1}^{RES}, s_{t}^{RES}, \cdots, s_{t-w+1}^{RES}\} \\ \hat{s}_{t+1} = LSTM\{s_{t-1}^{RES}, s_{t}^{RES}, \cdots, s_{t-w+1}^{RES}\} \end{cases} \tag{13}$$

From Equation (13), the data sequence is normalized before entering the LSTM model, as shown in Equation (14).

$$z_i^n = \frac{x_i^n - min(x)}{max(x) - min(x)}, n \in \{1, 2, \cdots, n\} \tag{14}$$

In Equation (14), the data sequence is reversed to eliminate the normalization effect when it is taken as the output signal. Then, the root-mean-square error (RMSE) and coefficient of determination (R^2) values are used to verify the prediction and model accuracy. The error (E_i) and mean absolute error (MAE) are also introduced for performance evaluation. The calculation procedures of the error evaluation metrics are expressed mathematically, as shown in Equation (15).

$$\begin{cases} E_i = RUL_i - \widehat{RUL}_i \\ MAE = \dfrac{1}{n}\displaystyle\sum_{i=1}^{n} |E_i| \end{cases} \tag{15}$$

In Equation (15), E_i is the prediction error or residual; RUL_i is the actual RUL of the battery system; $\widehat{RUL}_i$ is the predicted RUL value at each time point by the proposed model; n is the total number of data points.

The RMSE shows how dispersed the estimated error is away from the mean. The mathematical expression for the

calculation of the RMSE is shown in Equation (16).

$$RMSE = \sqrt{\frac{1}{n}\sum_{i=1}^{n}(E_i)^2} \tag{16}$$

The percentage-wise expression of the MAE is the MAPE. Its mathematical expression is shown in Equation (17).

$$MAPE = \frac{100\%}{n}\sum_{i=1}^{n}\left|\frac{RUL_i - \widehat{RUL}_i}{RUL_i}\right| \tag{17}$$

The R^2 value indicates the accuracy of a model to the actual RUL value, and it is scaled between 0 and 1. Its mathematical expression is shown in Equation (18).

$$R^2 = 1 - \frac{SS_{res}}{SS_{tot}} = 1 - \frac{\sum_{t=1}^{n}(RUL_i - \widehat{RUL}_i)^2}{\sum_{t=1}^{n}(RUL_i - \overline{RUL}_i)^2} \tag{18}$$

In Equation (18), SS_{res} is the sum of squares of residuals, and SS_{tot} is the total sum of squares. The other parameters have the same meaning as the previous error metrics.

3. Experimental analysis

According to the phased objectives, various dynamic working-condition RUL tests are carried out continuously. Considering the various influencing parameters, such as the effects of temperature, current rate, and cyclic charge-discharge time, the characteristics of the performance parameters are expounded at different energy stages. It reveals the effects of these influencing parameters on the battery packing mode, according to which a multi-stage fusion ECM is established by considering the internal multivariable coupling performance. A universal experimental verification is formed with a functional representation of external parameters based on the changing law of output characteristics under the influence of complex working conditions.

3.1. Battery attenuation and BBDST parametric initialization

When the activity of the battery increases, the positive and negative oxygen potentials decrease. Subsequently, when the current is varying, the voltage is low due to the fast charging reaction. The weakening of the charge-accepting ability leads

to the insufficient phenomenon. When the discharge current is large, the total battery power is low. The internal resistance decrease causes the multiple discharge current rates to increase, thus reaching the cut-off voltage fast. When the current inside the battery is large, the temperature rises and affects the power supply performance. However, when the discharge current is greater than the rated value, the internal polarization effect increases. The cut-off voltage is reached quickly, so the adoption rate and performance ratio drop sharply. It even leads to the deposition of lithium ions inside the battery, and the loss increases, which seriously affects the power capacity. The upper cut-off voltage facilitates the overcharge, resulting in a large amount of flammable gas, expansion, or even explosion. Subsequently, the irreversible electrochemical reaction occurs, which seriously affects the battery lifespan, so the testing procedure is designed along with the varying temperature and current rate conditions. The entire program design is shown in Figure 5.

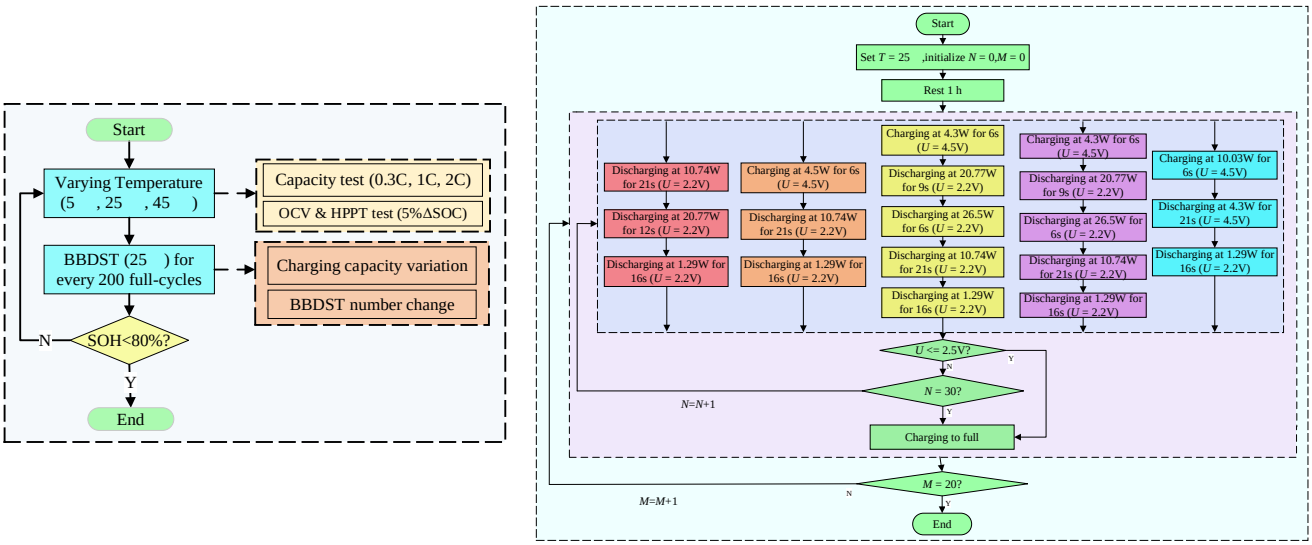

(a) Whole-life-cycle aging procedure (b) Testing procedure for the BBDST

Figure 5. Whole-life-cycle battery aging test procedure and BBDST

In Figure 5, the design of the whole-life-cycle test shows that the battery characteristics are obtained from two main steps, including the basic characteristic test of changing temperature and the BBDST. Consequently, different temperature conditions are considered for the basic characteristic test, including 5, 25, and 45°C. In this case, the capacity, OCV, and HPPC tests are performed in a chamber with controlled working environmental conditions. Then, the BBDST is checked with 10 total cycling tests, and there are almost 21 small pulse-current charge-discharge cycles. As for the whole-life-cycle

test of the cyclic charge-discharge conditions, specific implementation steps are designed for the BBDST. The battery pack placed in one electric car is characterized by b and the battery cell is characterized by c, so the SOP value of each battery cell can be obtained from the battery pack, as shown in Equation (19).

$$P_c^{'} = \alpha P_c = \alpha \frac{U_c Q_c}{U_c Q_c} P_b = \alpha \lambda_b P_b \tag{19}$$

In Equation (19), λ_b is the equivalent coefficient; α is the overload capacity factor to expand the test power to obtain the overloading capacity. The initial voltage value of the battery pack in the EV is 384 V, and the rated capacity is 360 Ah. Since the normal voltage of the battery cell is 3.60 V and the rated capacity is 2.2 Ah, the power calculation process can be obtained by setting α=5, as shown in Equation (20).

$$P_c^{'} = \alpha \frac{U_c Q_c}{U_c Q_c} P_b = 5 \times \frac{3.6 \times 2.2}{384 \times 360} \times P_b = 2.8646 \times 10^{-4} \times P_b \tag{20}$$

In Equation (20), after the CC-CV charging, the BBDST is conducted to repeat the main discharge step until the CCV drops to the cut-off voltage value. Then, the charge-discharge test power is calculated accordingly. The average current rate is 1 C, which can be calculated by $I = P/U$ by taking $U = 3.6$ V. Every time, the BBDST is performed for 300 s and the test lasts 12 times to fully discharge the battery. Then, the procedure turns out to be the CC-CV charging with a current rate of 0.5 C. A single BBDST time of the pulse-current charge-discharge treatment is 1 hour, and another charge time is 2.5 hours, making a total testing time of 3.5 hours. Considering the size of the data file, 1 file can be formed in 3 days for high efficiency, so the calculation formula for the cycling number is 24×3 / 3.5≈20. The iterative calculation procedure is mixed with theoretical steps to verify the testing results. Then, the dynamic loop test influence is considered to analyze the output factor of the measured data. The initial value is calibrated through adaptive parameter identification to verify the accuracy, robustness, and real-time performance.

3.2. Whole-life-cycle BBDST and RPT results

The whole-life-cycle BBDST working condition test is designed and realized for 1200 charge-discharge cycles at an

ambient temperature of 25 ℃. For every 20 cycles, a testing data file is formed, and the battery characteristic tests are conducted for the reference performance test (RPT), including the capacity determination, OCV, and HPPC tests. The characteristic analysis is also conducted at various temperatures, which are 5, 25, and 45 °C. The capacity test is conducted using current rates of 0.3, 1, and 2 C. The OCV and HPPC tests are conducted for every 5% SOC decreasing internally from 100 to 0%. The cyclic BBDST and RPT are conducted until the SOH value reaches 80%, as shown in Figure 6.

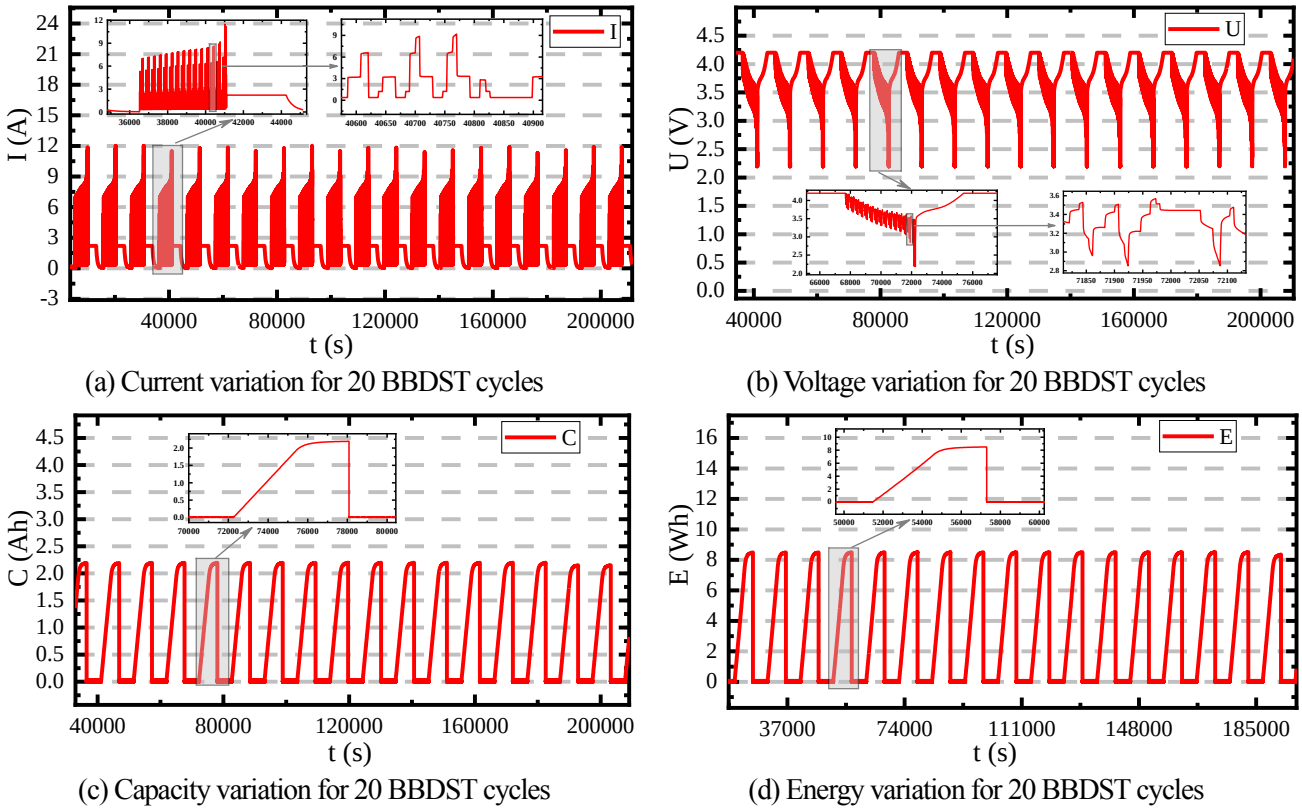

(a) Current variation for 20 BBDST cycles

(b) Voltage variation for 20 BBDST cycles

(c) Capacity variation for 20 BBDST cycles

(d) Energy variation for 20 BBDST cycles

Figure 6. The RPT determination for the 20-BBDST cycle

In Figure 6, for every 20-BBDST cycle, the experimental results are recorded, including current, voltage, capacity, and energy variations. The current variation is designed as shown in subfigure (a), in which 20 BBDST cycles are conducted for each single-file experimental test; the corresponding voltage variation is shown in subfigure (b); the corresponding capacity variation is shown in subfigure (c), and the corresponding energy variation is shown in subfigure (d). Then, the capacity determination, HPPC, and OCV variation testing results are obtained by conducting the RPT, as shown in Figure 7.

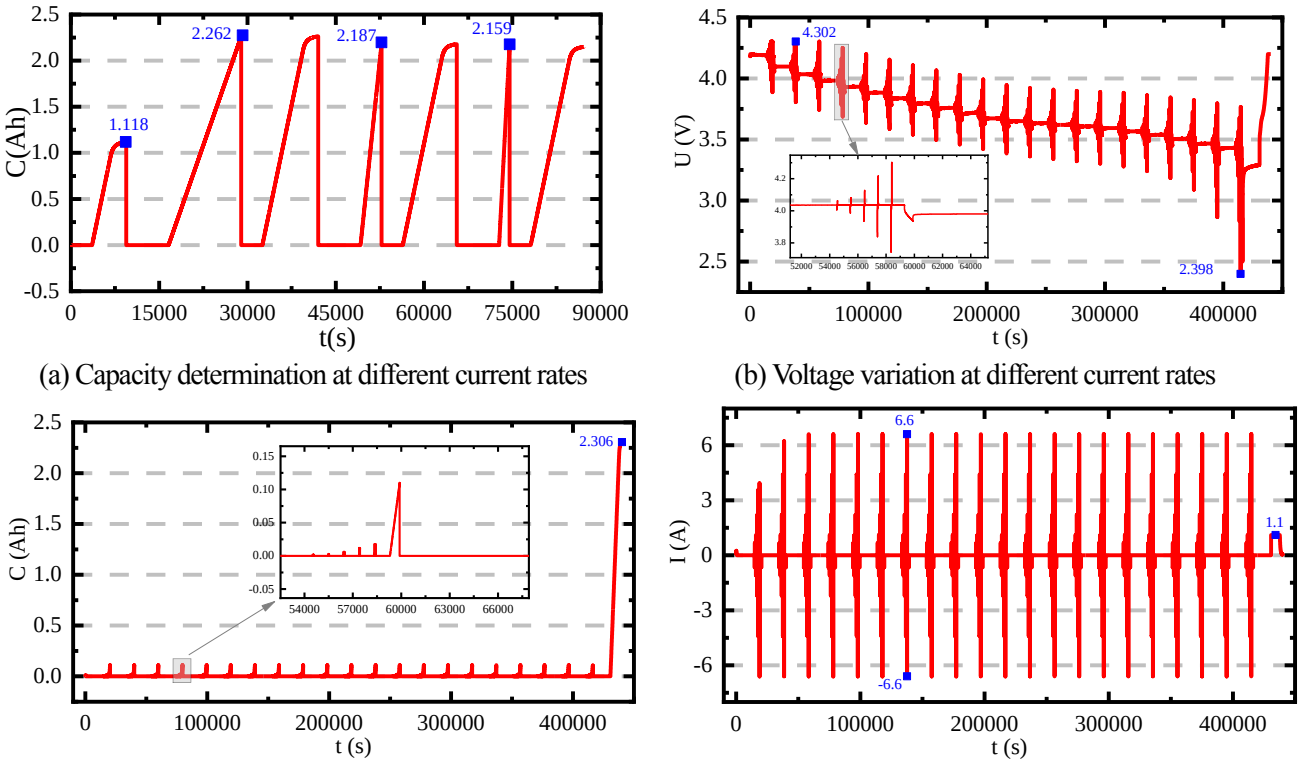

(a) Capacity determination at different current rates

(b) Voltage variation at different current rates

(c) Capacity variation for the whole cycle life test

(d) Current variations and supplementary charging tests

Figure 7. The RPT determination for every 20-HPPC cycle test

In Figure 7, the capacity determination order is designed, as shown in subfigure (a), in which three full charge-discharge cycle tests are conducted. The voltage variation for the HPPC tests is plotted, as shown in subfigure (b), in which 20 BBDST cycles are conducted for every 5% SOC variation. The corresponding capacity variation is shown in subfigure (c). The current variation and determination are plotted, as shown in subfigure (d). After the whole-life-cycle BBDST, the detailed experimental data is obtained and shared on the website: https://www.researchgate.net/project/Battery-life-test.

3.3. Capacity fading effect in the cyclic BBDST

For the capacity fading process, the measured capacity values are recorded and selected from the original data. The capacity variation for the BBDST is obtained for different temperature, current, and SOH conditions, as shown in Table 1.

Table 1. The cyclic BBDST capacity variation for battery *C*7

SOH (%)	*T* (°C)	C-rate	*C* (Ah)	SOH (%)	*T* (°C)	*Cr* (1.00)	*C* (Ah)
100	5	0.30	2.079	85	25	2.00	1.476
100	5	1.00	1.999	80	25	0.30	1.404
100	5	2.00	2.006	80	25	1.00	1.157
95	5	0.30	1.932	80	25	2.00	1.016
95	5	1.00	1.820	75	25	0.30	1.089

95	5	2.00	1.790	75	25	1.00	0.851
90	5	0.30	1.776	75	25	2.00	0.641
90	5	1.00	1.639	70	25	0.30	1.018
90	5	2.00	1.599	70	25	1.00	0.710
85	5	0.30	1.528	70	25	2.00	0.354
85	5	1.00	1.375	100	45	0.30	2.360
85	5	2.00	1.323	100	45	1.00	2.340
100	25	0.30	2.262	100	45	2.00	2.325
100	25	1.00	2.187	95	45	0.30	2.197
100	25	2.00	2.159	95	45	1.00	2.159
95	25	0.30	2.113	95	45	2.00	2.123
95	25	1.00	2.019	90	45	0.30	2.031
95	25	2.00	1.977	90	45	1.00	1.961
90	25	0.30	1.932	90	45	2.00	1.905
90	25	1.00	1.836	85	45	0.30	1.694
90	25	2.00	1.779	85	45	1.00	1.580
85	25	0.30	1.661	85	45	2.00	1.540
85	25	1.00	1.540	-	-	-	-

In Table 1, SOH is the calculated health level as an evaluation factor that is obtained from the battery manufacturer and cycle number, and T is the ambient temperature under which the experiment is conducted. C-rate is the charge-discharge current rate, and C is the capacity for the corresponding testing conditions.

Table 2 The cyclic HPPC test capacity variation for battery *C*7

SOH (%)	T (°C)	C-rate	C (Ah)	SOH (%)	T (°C)	Cr (1.00)	C (Ah)
100	5	0.30	2102	85	25	2.00	1.504
100	5	1.00	1.931	80	25	0.30	1.395
100	5	2.00	2.023	80	25	1.00	1.157
95	5	0.30	1.932	80	25	2.00	1.003
95	5	1.00	1.791	75	25	0.30	1.074
95	5	2.00	1.786	75	25	1.00	0.843
90	5	0.30	1.762	75	25	2.00	0.632
90	5	1.00	1.597	70	25	0.30	1.009
90	5	2.00	1.602	70	25	1.00	0.697
85	5	0.30	1.547	70	25	2.00	0.362
85	5	1.00	1.416	100	45	0.30	2.352
85	5	2.00	1.311	100	45	1.00	2.297
100	25	0.30	2.197	100	45	2.00	2.216
100	25	1.00	2.201	95	45	0.30	2.189
100	25	2.00	2.163	95	45	1.00	2.161
95	25	0.30	2.109	95	45	2.00	2.118
95	25	1.00	2.007	90	45	0.30	2.021
95	25	2.00	1.989	90	45	1.00	1.959
90	25	0.30	1.964	90	45	2.00	1.913
90	25	1.00	1.861	85	45	0.30	1.687
90	25	2.00	1.754	85	45	1.00	1.614

85	25	0.30	1.679	85	45	2.00	1.534
85	25	1.00	1.499	-	-	-	-

In addition, the capacity changes are obtained under the HPPC working condition for different temperatures, current rates, and SOH levels, as shown in Table 2 The cyclic HPPC test capacity variation for battery *C*7. Based on the recorded parameter values, the capacity fading process is expressed and used for the training of the constructed ANA-LSTM model.

3.4. Long-term RUL prediction effect for dynamic conditions

The cycle next to 90% of the initial capacity is taken as a fixed starting data point, and various failure threshold mechanisms are used for the RUL prediction to verify the effectiveness of the proposed ANA-LSTM model. The prediction results are obtained, and the RMSE values are compared. The model is trained on a single GPU, and the main data training time points during the LSTM training process are recorded, as shown in Table 3.

Table 3. The main data training time points during the LSTM training process

Epoch	Iteration	Time elapsed (hh:mm:ss)	Mini-batch RMSE	Mini-batch loss	Learning rate
1	1	00:00:02	0.820000	0.30000	0.0005000
13	50	00:00:05	0.100000	4.6e-03	0.0003000
25	100	00:00:07	0.010000	7.7e-05	0.0001000
38	150	00:00:09	0.060000	1.7e-03	7.5047e-05
50	200	00:00:11	8.66e-03	3.8e-05	3.9883e-05

In Table 3, the final mini-batch RMSE value demonstrates the effectiveness of the proposed ANA-LSTM model, which has minimum uncertainty with good efficiency and robustness. The RUL prediction result of the self-use dataset and B0007 of the National Aeronautics and Space Administration (NASA) with the RMSE and effective loss values under the DST working condition is recorded, as shown in Figure 8.

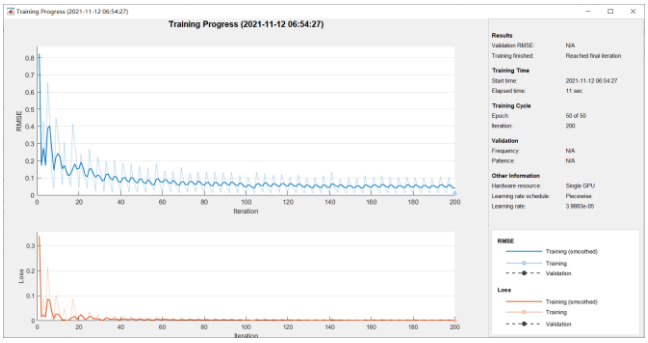

(a) ANA-LSTM RUL prediction of the self-use dataset training progress without noise

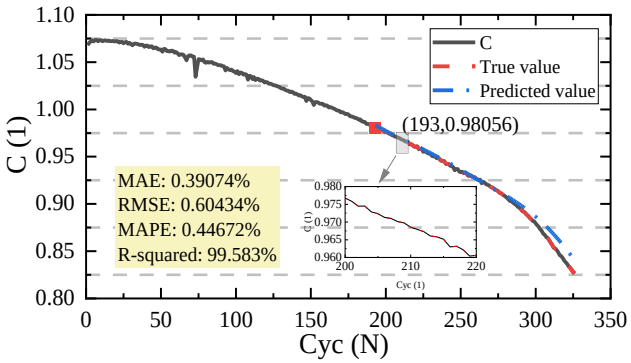

(b) RUL prediction result of the self-use dataset for practical training and testing without noise

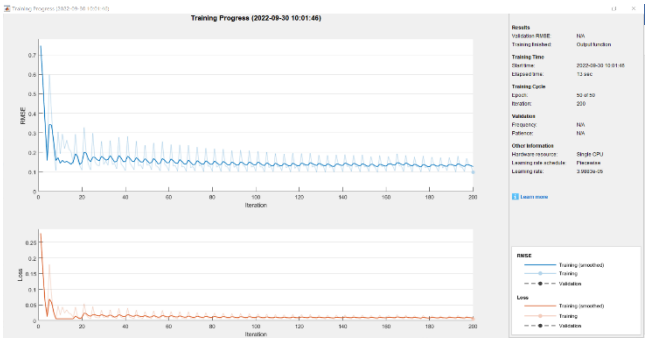

(c) ANA-LSTM RUL prediction of the self-use dataset training progress with noise

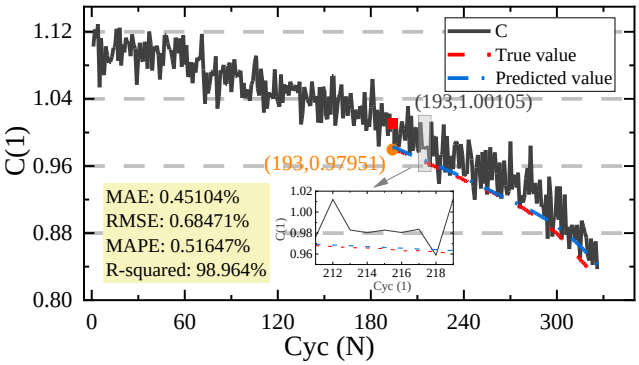

(d) RUL prediction result of the self-use dataset for practical training and testing with noise

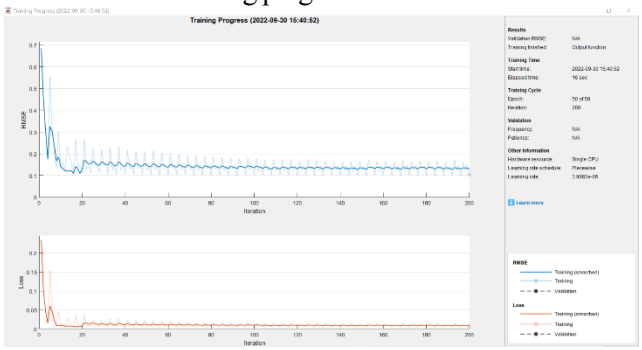

(e) ANA-LSTM RUL prediction of B0007 training progress with noise

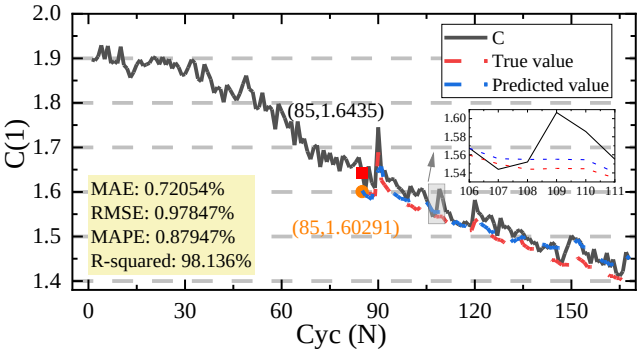

(f) RUL prediction result of B0007 for practical training and testing with noise

Figure 8. ANA-LSTM RUL prediction training progress and results under the DST working condition

Figure 8 (a), (c), and (e) show the performance of the LSTM RUL prediction training process without noise or with noise. Also, in subfigures (b), (d), and (f), *C* is the capacity degradation curve with the true and predicted RUL curves, and *C*_N refers to the capacity degradation curve with noise composed of white Gaussian noise and uniform noise. Both noises are at a 0.01 level. Also, the error values of the RUL prediction are defined in terms of MAE, RMSE, MAPE, and R^2. The true and predicted RUL values are compared using the absolute error in each inspection cycle, and the overall evaluation indicator is constructed for the prediction results. The error of the prediction result obtained by the ANA-LSTM model is the least in each inspection cycle, with an RMSE value of 0.60434%, MAE value of 0.39074%, MAPE value of 0.44672%, and the R^2 value of 0.99583. After the noise is added, the RMSE value is 0.68471%, the MAE value is 0.45104%, the MAPE value is 0.51647%, and the R2 value is 0.98964. In the RUL prediction for B0007, the RMSE value is 0.72054%, the MAE value is 0.97847%, the MAPE value is 0.87947%, and the *R*2 value is 0.98136. It shows that this method still retains high accuracy when dealing with data with obvious noise influence. All the model parameters are updated adaptively by the online measurement, according to which the capacity degradation uncertainty is captured effectively for complex working

conditions.

To further prove the accuracy and robustness of the proposed method, the most commonly used recurrent neural network (RNN), the original LSTM, and the newly proposed improved LSTM algorithm are selected, including the long short-term memory domain adaptation (LSTM-DA) presented by Han et al. [56] and the differential evolution grey wolf optimizer long short-term memory (DEGWO-LSTM) model proposed by Ma et al. [57]. The RMSE, MAE, MAPE, R^2, training and testing times, and convergence times of RUL prediction results are compared, and the results are shown in Table 4.

Table 4. Comparison of estimation results for B0007 with noise between the ANA-LSTM and other existing methods

Methods	RMSE (%)	MAE (%)	MAPE (%)	R^2 (1)	Training time (s)	Testing time (s)	Convergence times (s)
ANA-LSTM	0.97847	0.72054	0.87947	0.98136	11.56184	7.69392	3.48716
RNN	2.37468	1.16984	1.93412	0.90367	15.12385	11.64612	9.67456
LSTM	2.24210	1.07458	1.69748	0.92874	14.21875	10.15784	7.59212
LSTM-DA	2.03000	-	1.33000	-	13.74000	9.34000	6.12000
DEGWO-LSTM	1.63610	0.98640	1.14780	0.94264	12.97000	10.93000	5.71000

As can be seen from Table 4, the RMSE of the ANA-LSTM model is the lowest compared with other models, which decreases by 51.80% compared to the LSTM-DA model and 40.19% compared to the DEGWA-LSTM model. The MAE of the ANA-LSTM model decreases by 26.95% compared with the DEGWA-LSTM model, and the MAPE decreases by 33.87% and 23.38%, respectively. The R^2 increases by 4.11% compared to the DEGWA-LSTM model. The training times of the ANA-LSTM model reduce by 15.85% and 10.86%, respectively. The testing times decrease by 17.62% and 29.61%, respectively, and convergence times reduce by 43.02% and 38.93%, respectively. From the experimental tests, it can be observed that the ANA-LSTM-based RUL prediction result has the optimal accuracy with the least uncertainty, which verifies its accuracy and robustness.

4. Conclusion

A novel ANA-LSTM model is proposed to obtain the optimal expression to solve the robust RUL prediction problem. The model construction and adaptive feedback correction methods are employed for the high-precision RUL prediction, considering the current rate, ambient temperature, and other influencing factors, combining multiple feature coordination

mechanisms. A collaborative multi-parameter optimization is carried out based on the model training and meta-structure fine-tuning strategies. A new exploration of the RUL prediction method is realized by forming a new theory of battery system modeling, which optimizes the designing, manufacturing, and operation management of the battery effectively. Compared with the traditional data-driven methods, the proposed ANA-LSTM model achieves a high-precision RUL prediction effect with an RMSE value of 0.60434%, MAE value of 0.39074%, MAPE value of 0.44672%, and an R^2 value of 0.99583. This work accelerates the development of life cycle and intelligent management systems, providing theoretical support for the growth of lithium-ion battery systems.

This paper establishes an effective RUL prediction method based on anti-noise theory and a data-driven model, which provides a reasonable idea for further effective health management and further application of lithium-ion batteries. The next research direction mainly includes: Firstly, various factors that may affect the battery decay rate will be further considered, including internal factors such as charge/discharge ratio and external factors like pressure and air humidity. Secondly, the changes in internal resistance and capacity during the process of battery decay are comprehensively analyzed to obtain the response effect of the two to battery aging. Finally, the aging mechanism and RUL prediction of batteries will be further researched at the system level.

Acknowledgments

The work was supported by the National Natural Science Foundation of China (No. 62173281, 61801407), Sichuan Science and Technology Program (No. 2019YFG0427), China Scholarship Council (No. 201908515099), and Fund of Robot Technology used for Special Environment Key Laboratory of Sichuan Province (No. 18kftk03). Thanks to these sponsors.

Competing Interests

The authors declare no competing financial or non-financial interests.

Author Contribution

Shunli Wang: Conceptualization, methodology, and software.

Yongcun Fan: Data curation, writing, and original draft preparation.

Siyu Jin: Visualization and investigation.

Paul Takyi-Aninakwa: Software and validation.

Carlos Fernandez: Writing, reviewing, and editing.

Data Availability

All data included in this study are available upon request by contact with the corresponding author.

Reference

1. Ardeshiri, R.R., M. Liu, and C. Ma, *Multivariate stacked bidirectional long short term memory for lithium-ion battery health management.* Reliability Engineering & System Safety, 2022. **224**(2): p. 1-19.
2. Li, S., H. Fang, and B. Shi, *Remaining useful life estimation of Lithium-ion battery based on interacting multiple model particle filter and support vector regression.* Reliability Engineering & System Safety, 2021. **210**: p. 1-14.
3. Xu, T., Z. Peng, and L. Wu, *A novel data-driven method for predicting the circulating capacity of lithium-ion battery under random variable current.* Energy, 2021. **218**(119530): p. 1-13.
4. Sun, B.X., et al., *Study of Parameters Identification Method of Li-Ion Battery Model for EV Power Profile Based on Transient Characteristics Data.* IEEE Transactions on Intelligent Transportation Systems, 2021. **22**(1): p. 661-672.
5. Seruga, D., et al., *Continuous modelling of cyclic ageing for lithium-ion batteries.* Energy, 2021. **215**(119079): p. 1-14.
6. Sadabadi, K.K., X. Jin, and G. Rizzoni, *Prediction of remaining useful life for a composite electrode lithium ion battery cell using an electrochemical model to estimate the state of health.* Journal of Power Sources, 2021. **481**.
7. Ma, J., et al., *A hybrid transfer learning scheme for remaining useful life prediction and cycle life test optimization of different formulation Li-ion power batteries.* Applied Energy, 2021. **282**(116167): p. 1-17.
8. Gao, H.D., L.R. Cui, and Q.L. Dong, *Reliability modeling for a two-phase degradation system with a change point based on a Wiener process.* Reliability Engineering & System Safety, 2020. **193**: p. 1-13.
9. Tang, T. and H. Yuan, *A hybrid approach based on decomposition algorithm and neural network for remaining useful life prediction of lithium-ion battery.* Reliability Engineering & System Safety, 2022. **217**: p. 1-13.
10. Sierra, G., et al., *Battery health management for small-size rotary-wing electric unmanned aerial vehicles: An efficient approach for constrained computing platforms.* Reliability Engineering & System Safety, 2019. **182**: p. 166-178.
11. Downey, A., et al., *Physics-based prognostics of lithium-ion battery using non-linear least squares with dynamic bounds.* Reliability Engineering & System Safety, 2019. **182**: p. 1-12.
12. Liu, K.L., et al., *A Data-Driven Approach With Uncertainty Quantification for Predicting Future Capacities and Remaining Useful Life of Lithium-ion Battery.* IEEE Transactions on Industrial Electronics, 2021. **68**(4): p. 3170-3180.
13. Li, W., et al., *Online capacity estimation of lithium-ion batteries with deep long short-term memory networks.* Journal of Power Sources, 2021. **482**(228863): p. 1-11.
14. Chen, L., et al., *Battery state-of-health estimation based on a metabolic extreme learning machine combining degradation state model and error compensation.* Energy, 2021. **215**(119078): p. 1-10.

15. Zhu, S.X., et al., *A novel embedded method for in-situ measuring internal multi-point temperatures of lithium ion batteries.* Journal of Power Sources, 2020. **456**(16): p. 1-13.
16. Lee, C., et al., *Capacity-Fading Behavior Analysis for Early Detection of Unhealthy Li-Ion Batteries.* IEEE Transactions on Industrial Electronics, 2021. **68**(3): p. 2659-2666.
17. Kwak, E., et al., *Prediction of compression force evolution over degradation for a lithium-ion battery.* Journal of Power Sources, 2021. **483**(229079): p. 1-11.
18. Hossain Lipu, M.S., et al., *Intelligent algorithms and control strategies for battery management system in electric vehicles: Progress, challenges and future outlook.* Journal of Cleaner Production, 2021. **292**(126044): p. 1-27.
19. Liu, Y.G., et al., *Rule learning based energy management strategy of fuel cell hybrid vehicles considering multi-objective optimization.* Energy, 2020. **207**: p. 1-12.
20. Zhang, K., et al., *Remaining useful life prediction of aircraft lithium-ion batteries based on F-distribution particle filter and kernel smoothing algorithm.* Chinese Journal of Aeronautics, 2020. **33**(5): p. 1517-1531.
21. Zhang, H., et al., *Nonlinear-Drifted Fractional Brownian Motion With Multiple Hidden State Variables for Remaining Useful Life Prediction of Lithium-Ion Batteries.* IEEE Transactions on Reliability, 2020. **69**(2): p. 768-780.
22. Qiu, X.H., W.X. Wu, and S.F. Wang, *Remaining useful life prediction of lithium-ion battery based on improved cuckoo search particle filter and a novel state of charge estimation method.* Journal of Power Sources, 2020. **450**(227700): p. 1-13.
23. Cong, X., et al., *A Hybrid Method for the Prediction of the Remaining Useful Life of Lithium-Ion Batteries With Accelerated Capacity Degradation.* IEEE Transactions on Vehicular Technology, 2020. **69**(11): p. 12775-12785.
24. Ma, J., et al., *Cycle life test optimization for different Li-ion power battery formulations using a hybrid remaining-useful-life prediction method.* Applied Energy, 2020. **262**(114490): p. 1-16.
25. Zhou, Y.P., M.H. Huang, and M. Pecht, *Remaining useful life estimation of lithium-ion cells based on k-nearest neighbor regression with differential evolution optimization.* Journal of Cleaner Production, 2020. **249**: p. 1-12.
26. Zhou, D., et al., *Research on online estimation of available capacity of lithium batteries based on daily charging data.* Journal of Power Sources, 2020. **451**(227713): p. 1-16.
27. Chen, L., et al., *Remaining Useful Life Prediction of Battery Using a Novel Indicator and Framework With Fractional Grey Model and Unscented Particle Filter.* IEEE Transactions on Power Electronics, 2020. **35**(6): p. 5850-5859.
28. Li, X.Y., C.G. Yuan, and Z.P. Wang, *Multi-time-scale framework for prognostic health condition of lithium battery using modified Gaussian process regression and nonlinear regression.* Journal of Power Sources, 2020. **467**(228358): p. 1-12.
29. Zhao, M.H., et al., *Deep Residual Networks With Adaptively Parametric Rectifier Linear Units for Fault Diagnosis.* IEEE Transactions on Industrial Electronics, 2021. **68**(3): p. 2587-2597.
30. Wu, J., et al., *Battery-Involved Energy Management for Hybrid Electric Bus Based on Expert-Assistance Deep Deterministic Policy Gradient Algorithm.* IEEE Transactions on Vehicular Technology, 2020. **69**(11): p. 12786-12796.
31. Liu, K.L., et al., *An evaluation study of different modelling techniques for calendar ageing prediction of lithium-ion batteries.* Renewable & Sustainable Energy Reviews, 2020. **131**(110017): p. 1-14.
32. Lin, C.-P., et al., *Battery state of health modeling and remaining useful life prediction through time series model.* Applied Energy, 2020. **275**(115338): p. 1-21.
33. Li, P., et al., *State-of-health estimation and remaining useful life prediction for the lithium-ion battery based on a variant long short term memory neural network.* Journal of Power Sources, 2020. **459**(228069): p. 1-12.
34. Song, Y., et al., *A hybrid statistical data-driven method for on-line joint state estimation of lithium-ion batteries.* Applied Energy, 2020. **261**(114408): p. 1-11.
35. Yang, R., et al., *Characterization of external short circuit faults in electric vehicle Li-ion battery packs and prediction using artificial neural networks.* Applied Energy, 2020. **260**(114253): p. 1-10.
36. Eleftheroglou, N., et al., *Intelligent data-driven prognostic methodologies for the real-time remaining useful life until the end-of-discharge estimation of the Lithium-Polymer batteries of unmanned aerial vehicles with uncertainty quantification.* Applied Energy, 2019. **254**(113677): p. 1-10.

37. Ma, Y., et al., *The capacity estimation and cycle life prediction of lithium-ion batteries using a new broad extreme learning machine approach.* Journal of Power Sources, 2020. **476**(228581): p. 1-11.
38. Chehade, A.A. and A.A. Hussein, *A Collaborative Gaussian Process Regression Model for Transfer Learning of Capacity Trends Between Li-Ion Battery Cells.* IEEE Transactions on Vehicular Technology, 2020. **69**(9): p. 9542-9552.
39. Xiang, S., et al., *Automatic multi-differential deep learning and its application to machine remaining useful life prediction.* Reliability Engineering & System Safety, 2022. **223**: p. 1-12.
40. Xu, X.D., et al., *Remaining Useful Life Prediction of Lithium-ion Batteries Based on Wiener Process Under Time-Varying Temperature Condition.* Reliability Engineering & System Safety, 2021. **214**: p. 12.
41. Liu, Y.G., et al., *Online energy management strategy of fuel cell hybrid electric vehicles based on rule learning.* Journal of Cleaner Production, 2020. **260**: p. 1-11.
42. Lian, R.Z., et al., *Rule-interposing deep reinforcement learning based energy management strategy for power-split hybrid electric vehicle.* Energy, 2020. **197**: p. 1-10.
43. Zraibi, B., et al., *Remaining Useful Life Assessment for Lithium-Ion Batteries Using CNN-LSTM-DNN Hybrid Method.* IEEE Transactions on Vehicular Technology, 2021. **70**(5): p. 4252-4261.
44. Zhang, Y., et al., *A Remaining Useful Life Prediction Method in the Early Stage of Stochastic Degradation Process.* IEEE Transactions on Circuits and Systems, 2021. **68**(6): p. 2027-2031.
45. Wang, Z., N. Liu, and Y. Guo, *Adaptive sliding window LSTM NN based RUL prediction for lithium-ion batteries integrating LTSA feature reconstruction.* Neurocomputing, 2021. **466**: p. 178-189.
46. Ren, L., et al., *A Data-Driven Auto-CNN-LSTM Prediction Model for Lithium-Ion Battery Remaining Useful Life.* IEEE Transactions on Industrial Informatics, 2021. **17**(5): p. 3478-3487.
47. Liu, K., et al., *A Data-Driven Approach With Uncertainty Quantification for Predicting Future Capacities and Remaining Useful Life of Lithium-ion Battery.* IEEE Transactions on Industrial Electronics, 2021. **68**(4): p. 3170-3180.
48. Li, D. and L. Yang, *Remaining Useful Life Prediction of Lithium Battery Based on Sequential CNN–LSTM Method.* Journal of Electrochemical Energy Conversion and Storage, 2021. **18**(4): p. 1-13.
49. Wang, S.L., et al., *A novel energy management strategy for the ternary lithium batteries based on the dynamic equivalent circuit modeling and differential Kalman filtering under time-varying conditions.* Journal of Power Sources, 2020. **450**: p. 1-36.
50. Jafari, M. and Z. Malekjamshidi, *Optimal energy management of a residential-based hybrid renewable energy system using rule-based real-time control and 2D dynamic programming optimization method.* Renewable Energy, 2020. **146**: p. 254-266.
51. Hu, X., et al., *A Particle Filter and Long Short-Term Memory Fusion Technique for Lithium-Ion Battery Remaining Useful Life Prediction.* Journal of Dynamic Systems Measurement and Control-Transactions of the Asme, 2021. **143**(6): p. 1-13.
52. Cheng, G., X. Wang, and Y. He, *Remaining useful life and state of health prediction for lithium batteries based on empirical mode decomposition and a long and short memory neural network.* Energy, 2021. **232**: p. 1-11.
53. Chen, J.C., et al., *Combining empirical mode decomposition and deep recurrent neural networks for predictive maintenance of lithium-ion battery.* Advanced Engineering Informatics, 2021. **50**: p. 1-23.
54. Wang, F.-K., C.-Y. Huang, and T. Mamo, *Ensemble Model Based on Stacked Long Short-Term Memory Model for Cycle Life Prediction of Lithium-Ion Batteries.* Applied Sciences-Basel, 2020. **10**(10): p. 1-12.
55. Li, X., et al., *Multi-state joint estimation for a lithium-ion hybrid capacitor over a wide temperature range.* Journal of Power Sources, 2020. **479**: p. 1-14.
56. Han, T., Z. Wang, and H. Meng, *End-to-end capacity estimation of Lithium-ion batteries with an enhanced long short-term memory network considering domain adaptation.* Journal of Power Sources, 2022. **520**.
57. Ma, Y., et al., *A novel method for state of health estimation of lithium-ion batteries based on improved LSTM and health indicators extraction.* Energy, 2022. **251**.